RESEARCH ARTICLE

Lithium Sulfur Batteries

Energy & Environmental Materials WILEY

Redox-Mediating Mo_2C Nanoparticles Confined Within Nitrogen- and Phosphorus-Codoped Amorphous Carbon Matrix for Lithium–Sulfur Batteries

*Won Il Kim, Min Ju Kim, Hyunyoung Park, Minjun Hwang, Jin Suk Byun, Jaeheon Lee, Jongsoon Kim, and Ho Seok Park**

Lithium–sulfur batteries (LSBs) suffer from sluggish lithium polysulfides (LiPS) conversion and severe interfacial instability, which limit their rate performance and cycle life. Herein, we report a multifunctional interlayer comprising Mo_2C nanoparticles confined within a nitrogen- and phosphorus-codoped amorphous carbon matrix supported on reduced graphene oxide (MNPG). $H_3PMo_{12}O_{40}$ was chosen as a final polyoxometalate (POM) precursor because it was transformed into the tubular nanoparticles, while $Na_3PMo_{12}O_{40}$ was converted to irregular micrometer-sized particles. In particular, the hierarchical structure of MNPG is synthesized via electrostatic self-assembly of POM and pyrrole on graphene oxide, followed by thermal transformation. The embedded Mo_2C domains act as efficient redox mediators that accelerate LiPS conversion, while the polar doped carbon shell suppresses parasitic reactions and facilitates ion transport. Consequently, the MNPG-coated separator allows LSBs to deliver a high specific capacity of 1549 mAh g^{-1} at 0.1 C and 802 mAh g^{-1} at 5.0 C, along with 81.1% capacity retention after 200 cycles. This study provides a straightforward and effective interfacial engineering strategy that combines redox-mediating domains and transport regulation within a unified structure to overcome key bottlenecks of LSBs.

1. Introduction

With the rapid development of urban air mobility and aerospace engineering, lithium–sulfur batteries (LSBs) are gathering increasing interest owing to their high theoretical energy density (2600 Wh kg^{-1}), which is suitable for applications requiring light weight.[1,2] However, achieving a practical level of LSBs is impeded by several challenges, namely the low intrinsic conductivity of S/Li_2S, substantial volume expansion during discharge/charge, sluggish lithium polysulfides (LiPS) conversion kinetics, and shuttle effect resulting from excessive LiPS dissolution.[3,4] To date, extensive strategies have been proposed to resolve the limitations, including structural modification of carbonaceous materials,[5,6] and electrocatalyst adjustment.[7,8]

Among them, transition metal-based redox mediators have been considered promising candidates for promoting LiPS conversion, owing to their strong polar interactions that effectively capture LiPS species.[9,10] In particular, molybdenum carbide (Mo_2C) has been investigated owing to its metallic conductivity and catalytic activity for the improved redox kinetics and the mitigation of shuttle effects.[11] However, the cycling stability with Mo_2C was not sufficiently high due to its polar sites vulnerable to continuous reaction with LiPS.[12] To address these issues, protective carbon layers have been introduced to passivate the surface of redox mediators while maintaining conductive pathways.[13] In particular, amorphous carbon is considered an adaptable alternative to graphitic coatings due to its abundant defect sites, enhanced surface polarity, flexibility, and favorable compatibility with nanostructured redox-mediators.[14,15] Carefully tuning thickness and morphology, such an amorphous carbon layer can function as a protective shield against undesired reactions, acting as a diffusion-regulating interface that guides LiPS transport in a controlled manner.[16] Furthermore, incorporating heteroatoms into the carbon matrix can further enhance its chemical affinity for LiPS and improve the interfacial stability of the composite.[17–19]

Herein, we report hierarchical composites consisting of Mo_2C nanoparticles embedded in a nitrogen- and phosphorus-codoped amorphous carbon matrix, supported on reduced graphene oxide. The resulting composite is denoted as MNPG, and the reduced graphene oxide

W. I. Kim, M. J. Kim, M. Hwang, J. S. Byun, J. Lee, Prof. H. S. Park
School of Chemical Engineering, College of Engineering, Sungkyunkwan University, Suwon 16419, Korea
E-mail: phs0727@skku.edu
H. Park, Prof. J. Kim
Department of Energy Science, Sungkyunkwan University, Suwon 16419, Korea
H. Park, Prof. J. Kim, Prof. H. S. Park
SKKU Institute of Energy Science and Technology (SIEST), Sungkyunkwan University, Suwon 16419, Korea
Prof. H. S. Park
Department of Health Sciences and Technology, Samsung Advanced Institute for Health Sciences and Technology (SAIHST), Sungkyunkwan University, Suwon 16419, Korea
SKKU Advanced Institute of Nano Technology (SAINT), Sungkyunkwan University, Suwon 16419, Korea
The ORCID identification number(s) for the author(s) of this article can be found under https://doi.org/10.1002/eem2.70156.

DOI: 10.1002/eem2.70156

support is hereafter referred to as G. The composite was synthesized by leveraging electrostatic interactions among polyoxometalates (POM), pyrrole, and graphene oxide, which spontaneously assembled into a precursor complex. Subsequent thermal treatment transformed the POM domains into crystalline Mo_2C while carbonizing the surrounding polymer network. The resulting structure features uniformly distributed Mo_2C nanoparticles confined within a nitrogen- and phosphorus-codoped amorphous carbon matrix that can further enhance its chemical affinity for LiPS. This configuration provides redox-mediating domain cores and a defect-rich carbon environment that facilitates LiPS conversion, suppresses side reactions, and regulates ion transport. Accordingly, LSBs incorporating a MNPG-modified separator exhibited a high specific capacity of 1549 mAh g^{-1} at 0.1 C and excellent rate capability of 802 mAh g^{-1} at 5.0 C. It also maintained a high capacity of 928.4 mAh g^{-1} after 200 cycles at 0.2 C, corresponding to high-capacity retention of 81.1% with a low-capacity fading rate of 0.095% per cycle.

2. Results and Discussion

Figure 1 presents a schematic illustration of the synthesis process for the MNPG composite. A polyoxometalate compound was employed as both a metal precursor and a self-assembly inducer.[20] Upon its introduction into a mixed solution of pyrrole and graphene oxide, the POM oxidizes pyrrole to form positively charged polypyrrole (ppy), while simultaneously engaging in electrostatic interactions as the negatively charged POM clusters.[21,22] These interactions drive the spontaneous self-assembly of hybrid POM/ppy nanoparticles on the graphene oxide surface. Subsequent thermal treatment induces the in situ transformation of POM into crystalline Mo_2C while concurrently carbonizing the surrounding ppy layer. Nitrogen and phosphorus atoms originating from ppy and POM, respectively, are incorporated into the carbon framework during thermal transformation, yielding a nitrogen- and phosphorus-codoped amorphous carbon matrix. The resulting MNPG architecture features Mo_2C nanoparticles uniformly confined within this heteroatom-codoped matrix and anchored onto a reduced graphene oxide (G) template. This hierarchical structure provides abundant redox-active sites, strong polar interactions, and high electrical conductivity, while effectively mitigating parasitic reactions caused by direct contact with polar LiPS species.

To confirm the morphology of the hierarchical structure synthesized through self-assembly and in situ transformation, scanning electron microscopy (SEM) was conducted (**Figure 2a** and Figure S1, Supporting Information). The SEM images reveal that 50 nm scale nanoparticles are assembled into tubular structures with a diameter of 200 nm and uniformly distributed across the G surface. Energy-dispersive spectroscopy (EDS) mapping further confirms the uniform presence of Mo, C, N, and P elements (Figure S2, Supporting Information), indicating successful incorporation of nitrogen and phosphorus atoms from the pyrrole and POM precursors into the carbon matrix. In addition, the Mo_2C content in the optimized composite was quantified to be 46.68 wt%, as summarized in Table S1, Supporting Information. Although EDS signals were similar when using sodium phosphomolybdate ($Na_3PMo_{12}O_{40}$), a different POM precursor, the tubular nanoparticles were only formed when using phosphomolybdic acid ($H_3PMo_{12}O_{40}$), which was selected as a final POM precursor to control the nanomorphology (Figure S3, Supporting Information). In contrast, the utilization of $Na_3PMo_{12}O_{40}$ led to irregular aggregation and the formation of micrometer-sized particles with poor distribution (Figure S4, Supporting Information). The compositions of pyrrole and POM were also regarded as critical parameters because excessive pyrrole promoted layered structures, while excessive POM led to thick surface coatings hindering self-assembly (Figure S5, Supporting Information). These aggregated structures are less favorable for redox mediators due to the limited surface exposure of active sites, whereas the uniform tubular architecture derived from the optimized precursor composition offers enhanced surface accessibility.

In addition, the pyrolysis temperature was optimized to form the desired hierarchical structure. According to previous reports,[21] POM and POM/ppy composites subjected to treatment at 500 °C primarily form MoO_2 phases (Figures S6 and S7a, Supporting Information). However, to ensure both improved LiPS conversion kinetics through the formation of highly conductive carbide phases and the confinement of redox-active sites within the carbon matrix, a thermal treatment at 900 °C was employed. Notably, excessive carbonization time at this temperature is attributed to the appearance of metallic Mo phases (Figure S7b, Supporting Information), which are not suitable for LiPS interaction due to their low polarity and poor affinity toward LiPS.

Transmission electron microscopy (TEM) analysis was employed to examine the microstructure of MNPG (Figure 2b). Dark-contrast particles embedded within the matrix—highlighted by yellow outlines—are observed corresponding to Mo_2C with an average particle size of 30 nm. These particles are surrounded by a relatively light-contrast shell, measuring 20 nm in thickness, which is assigned to an amorphous carbon layer formed during thermal transformation. The clear core-shell contrast observed in the image suggests that the Mo_2C nanoparticles are spatially confined within a protective carbon matrix, which is expected to prevent direct exposure to LiPS and enhance redox stability. The corresponding high-resolution TEM image in Figure 2c shows well-defined lattice fringes with an interplanar spacing of 0.23 nm, which can be indexed to the (121) plane of orthorhombic Mo_2C.[23,24] This observation aligns with the most intense diffraction peak in the X-ray diffraction (XRD) pattern at $2\theta = 39.4°$, confirming the preferential orientation or dominant exposure of the (121) crystalline plane (Figure 2g). In contrast, the amorphous carbon region adjacent to the Mo_2C domain exhibits no visible lattice fringes, consistent with its disordered structure. In other words, the absence of a distinct (002) graphitic peak in the XRD profile further supports this assignment to amorphous

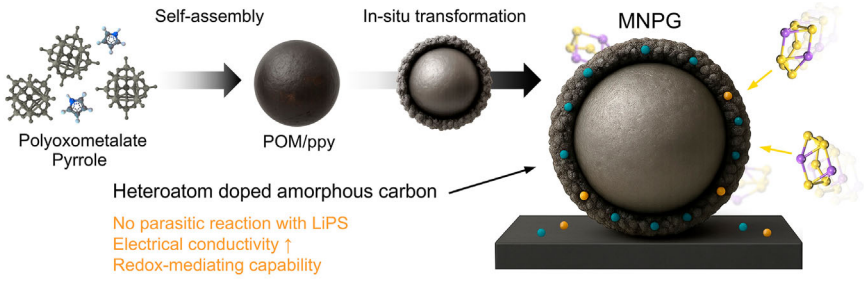

Figure 1. Schematic illustration about synthesis process and the function of MNPG.

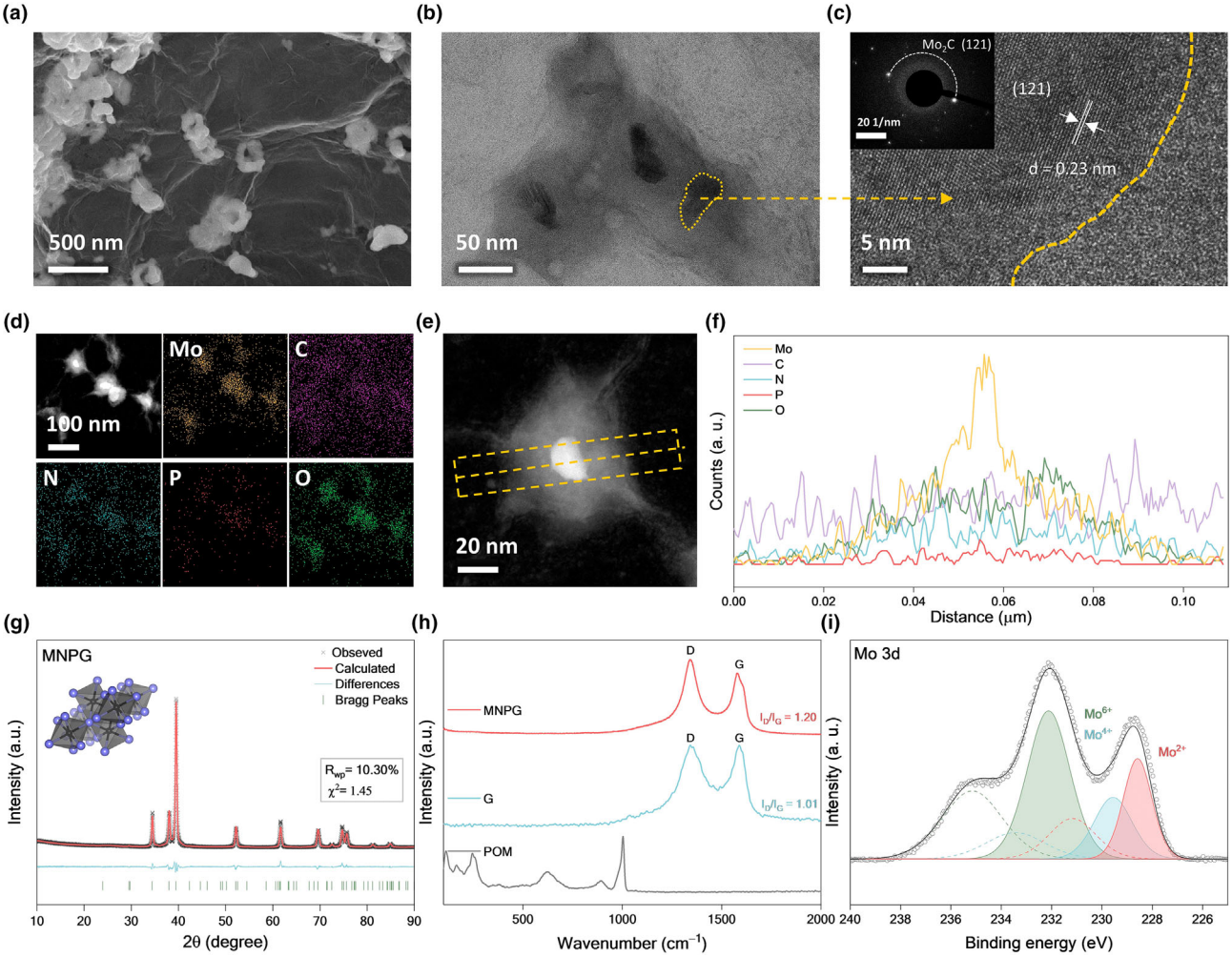

Figure 2. a) SEM images of MNPG. b) TEM image of MNPG. c) TEM image of MNPG with d-spacing and SAED pattern. d) Elemental mapping of MNPG confirming the uniform distribution of Mo, C, P, and N. e) STEM image of MNPG and the corresponding f) TEM-EDS line profile. g) Rietveld refinement of XRD of MNPG. h) Raman spectra of MNPG, G and POM. i) Mo 3d high-resolution XPS spectra of MNPG.

carbon. Furthermore, the selected area electron diffraction (SAED) pattern obtained from the same region displays sharp diffraction rings indexed to the (121) planes, further confirming the high crystallinity of the Mo_2C phase.

The EDS elemental mapping through TEM confirms that Mo_2C nanoparticles are homogeneously dispersed across the G surface, along with the uniform incorporation of nitrogen and phosphorus atoms into the surrounding carbon matrix (Figure 2d). This indicates successful heteroatom codoping derived from the pyrrole and POM precursors. In addition, the TEM-EDS line profile of a representative nanoparticle reveals a pronounced Mo signal concentrated at the core, indicating that the embedded nanoparticles are composed of Mo_2C (Figure 2e,f). A noticeable oxygen signal is also detected at the particle surface, which is attributed to partial surface oxidation of Mo during post-synthesis under air exposure. This is further supported by the Mo 3d X-ray photoelectron spectroscopy (XPS) results in Figure 2i, which display additional peaks corresponding to oxidized Mo species at the surface. However, no diffraction peaks of MoO_2 or MoO_3 are observed in the XRD pattern (Figure 2g), indicating that the bulk phase of the particles remains as pure Mo_2C. Collectively, these findings confirm the formation of well-defined Mo_2C nanodomains confined within a polar, heteroatom-doped carbon matrix, forming the fundamental redox-mediating architecture of the MNPG composite.

To further investigate the structural characteristics of MNPG, XRD and the associated Rietveld refinement analyses were conducted. As shown in Figure 2g and Table S2, Supporting Information, the Rietveld refinement of the MNPG reveals that it crystallizes in an orthorhombic Mo_2C phase with space group Pbcn (No. 60). These well-defined characteristic reflections confirm the successful formation of Mo_2C in the MNPG. The lattice parameters were determined to be $a = 4.741$ Å, $b = 6.023$ Å, and $c = 5.216$ Å, corresponding to a unit cell volume of 148.9472 Å^3. The refinement yielded acceptable reliability factors ($R_{wp} = 10.30\%$, $\chi^2 = 1.45$), indicating good agreement between the observed and calculated profiles. Various diffraction peaks observed at $2\theta = 34.4°$, 38.0°, 39.4°, 52.2°, 61.6°, 69.6°, 74.7°, 75.5°, 81.3°, and 84.7°, corresponding to the (002), (200), (121), (202), (023), (321), (223), (142), (400), and (242) planes, respectively, can be indexed to the orthorhombic Mo_2C phase (JCPDS No. 01-071-0242).

Notably, no peaks corresponding to residual POM precursors were detected, and the absence of the characteristic graphitic (002) peak near $2\theta \approx 26°$ further suggests the formation of an amorphous carbon layer surrounding the Mo_2C particles. The formation and metal complexation of MNPG were confirmed by Raman spectroscopy, in comparison to POM and G (Figure 2h). In the Raman spectra, both MNPG and G exhibited characteristic D and G bands at 1350 and 1580 cm^{-1}, respectively. The absence of peaks corresponding to the POM precursor indicates its complete removal after thermal treatment. The I_D/I_G ratio of G was 1.01, reflecting the partially restored sp^2 carbon domains in G.[25] In contrast, MNPG showed a higher I_D/I_G ratio of 1.20, suggesting the generation of polar surface defects and the formation of an amorphous carbon layer.

XPS was further employed to examine the chemical environment of MNPG (Figure 2i and Figures S8 and S9, Supporting Information). The high-resolution Mo 3d spectrum exhibited peaks at 228.1 and 231.3 eV, corresponding to Mo $3d_{5/2}$ and Mo $3d_{3/2}$ of Mo^{2+} species.[26] Although additional signals corresponding to Mo^{4+} and Mo^{6+} were observed, likely due to partial surface oxidation, the absence of MoO_2 and MoO_3 reflections in the XRD patterns confirms that only the surface of Mo_2C was oxidized. This is attributed to the thin and partially non-uniform amorphous carbon shell, which could not fully prevent air exposure. The C 1s spectrum was deconvoluted into C–C (284.6 eV), C–N (286.7 eV), C–P (285.7 eV), C=O (284.6 eV), and C–Mo (283.1 eV) components, indicating chemical bonding between Mo_2C and the carbon matrix.[27] The N 1s spectrum showed multiple nitrogen configurations, including pyridinic N (397.0 eV), pyrrolic N (398.8 eV), graphitic N (401.4 eV), and N–Mo (396.1 eV),[28] while the P 2p spectrum revealed P–C (133.1 eV) and P–O (134.4 eV) peaks,[29] confirming the successful incorporation of nitrogen and phosphorus atoms into the carbon structure. The presence of phosphorus atoms, which possess larger atomic size and stronger electron-donating capability compared to nitrogen, is expected to exert a synergistic effect, enabling efficient electron transport and providing abundant redox-mediating sites.[30] These heteroatoms generate polar sites on the surface, which enhance LiPS adsorption and contribute to improved electrochemical stability.

To better elucidate the redox-mediating capability of MNPG in the rate-determining step of the Li_2S precipitation process, potentiostatic discharge profiles were obtained in a 0.5 M Li_2S_8 electrolyte for both the MNPG and G electrodes (**Figure 3**a,b).[31] MNPG exhibited a high discharge capacity of 200.7 mAh g^{-1}, which is 1.7 times greater than that of G (119.6 mAh g^{-1}). Furthermore, MNPG showed a faster Li_2S deposition time of 5821 s with a higher response current compared to 7814 s of G, indicating the facilitated kinetics of Li_2S nucleation. These observations confirm that MNPG promoted electrochemical conversion kinetics of LiPS to Li_2S, enabling rapid and dense Li_2S deposition through redox mediating. The nucleation-promoting behavior of MNPG was further analyzed by comparing its current-time transients to theoretical electrochemical deposition models for Li_2S nucleation and growth (Figure 3c and Figure S10, Supporting Information). Based on the two-dimensional (2D) and three-dimensional (3D) nucleation growth models—namely the Bewick–Fleischmann–Thirsk (BFT) and Scharifker–Hills (SH) models—the dimensionless current-time profiles were fitted to assess the underlying Li_2S formation mechanism.[32] The G electrode displayed a nucleation behavior closely aligned with the 2D progressive (2DP) model, where Li_2S nuclei gradually evolve due to sparse active sites and weak LiPS affinity. In contrast, MNPG followed a 2D instantaneous (2DI) nucleation model, suggesting a high density of uniformly accessible nucleation sites, which is attributable to the enhanced LiPS conversion kinetics and the abundant electrochemically active surface provided by the MNPG.

To investigate the redox-mediating activity of MNPG toward LiPS, cyclic voltammetry (CV) was measured using a symmetric cell with MNPG electrodes in 0.5 M Li_2S_6 electrolyte (Figure 3d).[33] Three types of electrodes were compared: MNPG, featuring Mo_2C embedded within a heteroatom-doped amorphous carbon layer; MG, in which Mo_2C was simply deposited onto reduced graphene oxide without the carbon matrix; and G, the bare reduced graphene oxide. This comparison was designed to isolate and evaluate the individual contributions of the Mo_2C domains and the surrounding doped carbon layer. The CV profiles exhibited four distinct redox peaks. Peak a and b correspond to the reductions: solid-to-liquid phase transition from S_8 to LiPS (peak a), and the subsequent liquid-to-solid phase transition from LiPS to Li_2S (peak b). Peak c and d represent the reverse oxidation from Li_2S to LiPS (peak c) and LiPS to S_8 (peak d). Notably, the MNPG electrode exhibited the largest redox peak current with the smallest voltage polarization among the tested samples, outperforming both MG and G electrodes. This improvement is attributed to the synergistic effect of the heteroatom-doped amorphous carbon layer and the embedded Mo_2C redox-mediating domains. Furthermore, no current response was observed in a symmetric cell assembled without Li_2S_6 in the electrolyte, supporting the redox-mediating activity of MNPG on enhancing the LiPS conversion kinetics.

To evaluate the ability of MNPG to mitigate excessive LiPS dissolution, a visual adsorption test was conducted by immersing MNPG and G in a 5-mM Li_2S_6 solution (Figure 3e). After 24 h, the solution containing MNPG became noticeably clearer than that with G, indicating stronger LiPS adsorption by MNPG. To further investigate the chemical interaction between LiPS and the materials, XPS analysis was carried out.[20] Compared to G, the MNPG sample exhibited significantly stronger S 2p signals, revealing enhanced interactions with various LiPS species. Four characteristic sulfur doublets were identified: terminal sulfur (S_T, 163.3 and 165.1 eV), bridging sulfur (S_B, 164.1 and 165.8 eV), thiosulfate (168.7 and 170.2 eV), and polythionate (168.5 and 170.0 eV). The increased peak intensities across all species in the MNPG sample highlight its superior ability to capture and stabilize LiPS intermediates.

Density functional theory (DFT) calculations were subsequently performed to determine the role of heteroatom doping in governing the interactive chemistry between MNPG and LiPS (Figure 3f). The adsorption energy (E_a) was calculated using the following equation:

$$E_a = E_{surface/Li_2S_6} - (E_{surface} + E_{Li_2S_6}) \quad (1)$$

While DFT calculation cannot fully indicate the complex hierarchical structure of MNPG with amorphous carbon layer, a representative model was employed wherein a Mo_2C nanoparticle was embedded in the heteroatom-doped carbon substrate. In the result of MG without doping, the adsorption energy for Li_2S_6 was calculated to be −1.59 eV, indicative of weak adsorption dominated by van der Waals interactions. In contrast, the introduction of dopants significantly improved the interaction strength. For the nitrogen-doped system (MNG), the adsorption energy was enhanced to −2.08 eV, which is attributed to the formation of localized electron-deficient regions induced by the high electronegativity of nitrogen, thereby strengthening the electrostatic

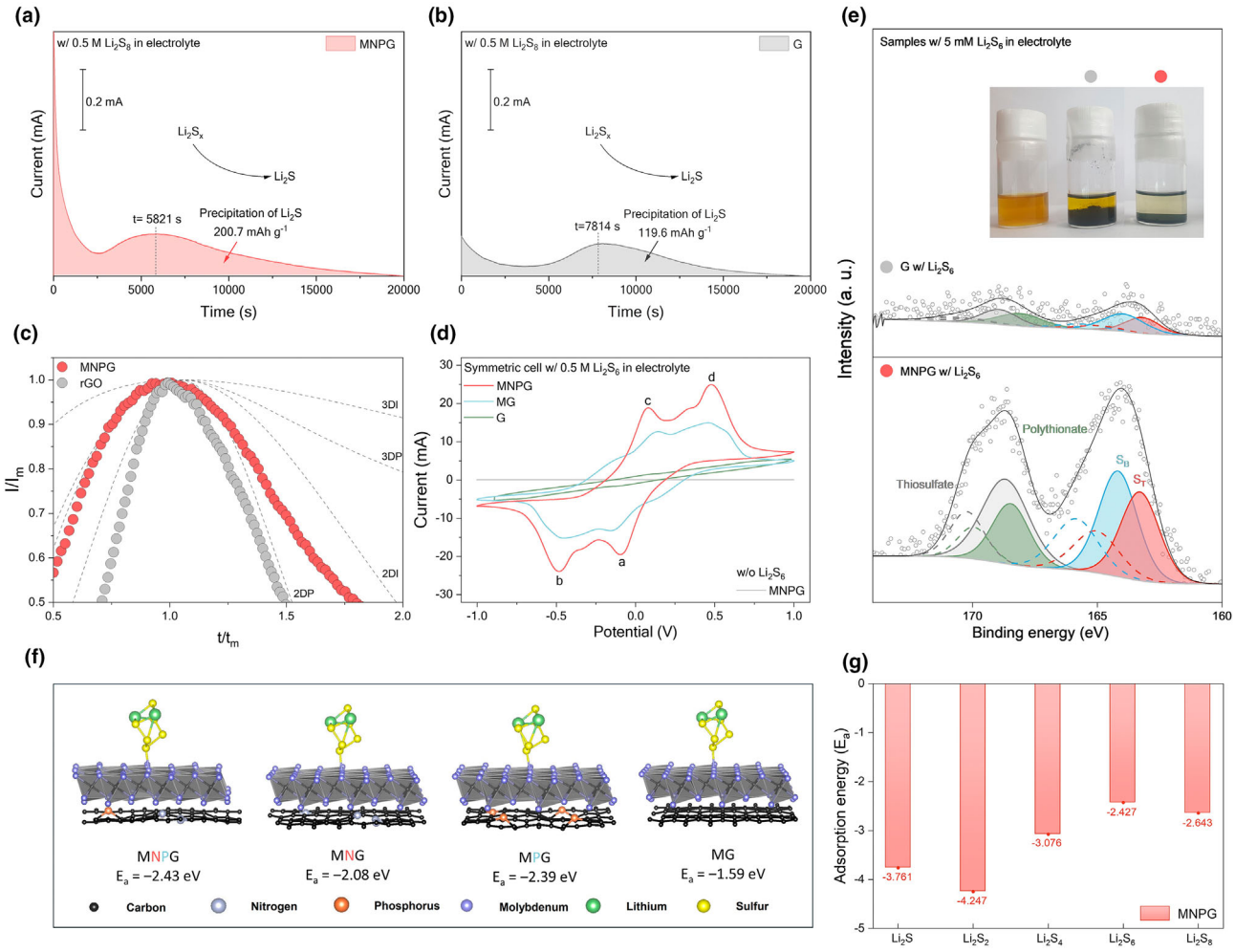

Figure 3. a) Potentiostatic discharge curves of using a 0.5 M Li_2S_8 solution at 2.09 V with MNPG and b) G. c) Corresponding dimensionless transient in comparison with theoretical nucleation models. d) CV curves of Li_2S_6 symmetric cells containing 0.5 M Li_2S_6 as the electrolyte at the scan rate of 5 mV s^{-1} within a voltage range of −1.0 to 1.0 V. e) S 2p high-resolution XPS spectra of G and MNPG after the polysulfide (Li_2S_6) adsorption test and image of Li_2S_6 absorption tests. f) DFT calculation of Li_2S_6 adsorption configurations and binding energies on various doped carbon matrix. g) DFT calculation of intermediate species adsorption energies on MNPG.

interaction with Li-ion.[34] Phosphorus-doping resulted in a further increase in E_a to −2.39 eV, which is due to the relatively low electronegativity and high electron-donating capability of phosphorus, promoting stronger LiPS binding.[35] Most notably, the co-doped MNPG structure exhibited the strongest adsorption energy of −2.43 eV. This enhanced interaction stems from the synergistic coexistence of N-induced electron-deficient sites and P-enriched electron-donating regions, collectively enabling robust binding of Li_2S_6 species. These findings confirm that heteroatom doping plays a critical role in modulating LiPS affinity, and that the co-doped MNPG structure provides the most favorable redox-mediating environment among the evaluated systems. Moreover, MNPG exhibited moderately strong adsorption energies not only toward Li_2S_6 but also across various intermediate species (Figure 3g). Compared to MoO_2 supported on N,P-codoped reduced graphene oxide (MoO_2 NPG), MNPG showed consistently stronger interactions throughout the entire LiPS conversion pathway, highlighting the advantage of the embedded Mo_2C and heteroatom doping in enhancing redox-mediating capability (Figure S11, Supporting Information).

To validate the redox-mediating capability of the MNPG—synthesized via self-assembly and in situ transformation—into a LSBs system, the material was applied as a functional interlayer by coating it onto a polypropylene (PP) separator.[36,37] The resulting modified separator is hereafter denoted as MNPG PP. This approach not only enables direct electrochemical interaction between the MNPG structure and migrating LiPS species but also decouples its redox-mediating function from the influence of the cathode composition. Focused ion beam–scanning electron microscopy (FIB-SEM) cross-sectional imaging (**Figure 4a**) revealed a uniformly deposited MNPG layer with a thickness of approximately 8.2 μm on the PP substrate. The impact of MNPG coating on interfacial electrolyte wettability was further assessed by contact angle measurements (Figure 4b,c). Compared to the pristine PP, which exhibited a high contact angle of 41°, the MNPG PP showed a significantly reduced contact angle of 13°, demonstrating enhanced affinity

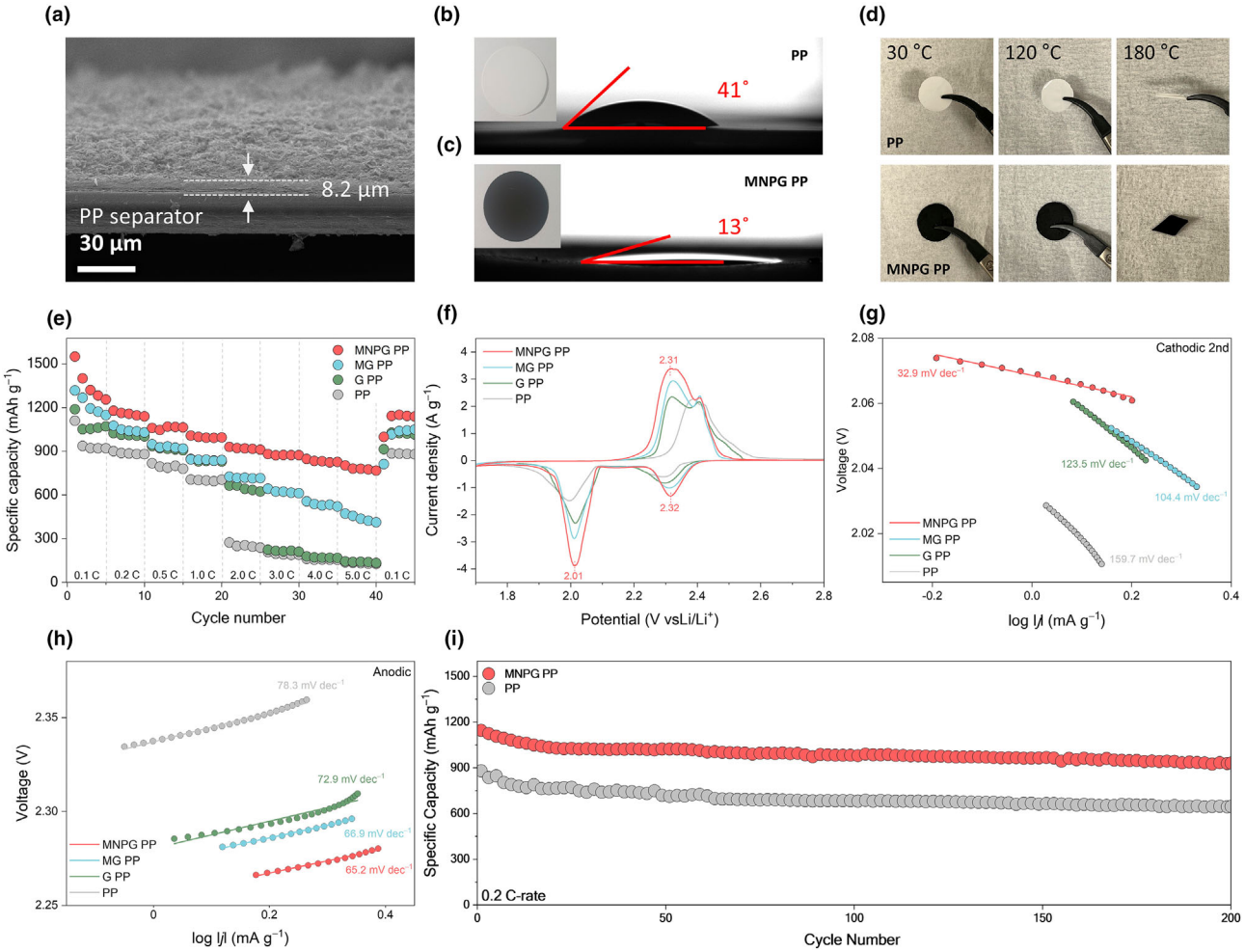

Figure 4. a) Cross-sectional FIB-SEM image of MNPG coated PP separator. b) Contact angle measurements on PP and c) MNPG PP. d) Images of each separator after heat treatment at various temperatures. e) Rate capability of MNPG PP, MG PP, G PP, and PP from 0.1 to 5.0 C. f) CV curves of the first cycle at 0.1 mV s^{-1} for MNPG PP, MG PP, G PP, and PP. Tafel plots calculated from g) cathodic second peak and h) anodic peak for MNPG PP, MG PP, G PP, and PP. i) Cycle performance of MNPG PP and PP at 0.2 C.

toward the electrolyte. The improved wettability is primarily attributed to the polar functional groups and heteroatom dopants present in the MNPG coating, which increase surface energy and facilitate favorable interactions with the electrolyte components. In addition to interfacial modification, the thermal stability of the separators was evaluated by observing their dimensional changes under elevated temperatures, as shown in Figure 4d. The pristine PP underwent visible shrinkage and deformation at higher temperatures, whereas MNPG PP moderately retained its structural integrity even at 180 °C. Additionally, MNPG PP exhibited strong adhesion and flexibility without delamination or cracking after repeated folding (Figure S12, Supporting Information). Furthermore, Li/Li symmetric cells with MNPG PP exhibited significantly improved interfacial stability, showing lower overpotentials and prolonged cycling performance compared to those with pristine PP, confirming its effectiveness in stabilizing Li metal deposition (Figure S13, Supporting Information).

The electrochemical performance of LSBs assembled with different separators (MNPG PP, MG PP, G PP and PP) was systematically evaluated, where carbon nanotube/sulfur composites (CNT-S) with a sulfur content of 76 wt% were prepared as the cathode by a melt-diffusion method (Figures S14 and S15, Supporting Information). The rate capability tests were conducted under various C-rates ranging from 0.1 to 5.0 C, followed by recovery cycles at 0.1 C (Figure 4e and Figure S16, Supporting Information). The cell with MNPG PP displayed the highest specific capacities of 1549, 1178, 1059, 1007, 920, 882, 847, and 802 mAh g^{-1} at the various C-rates of 0.1, 0.2, 0.5, 1.0, 2.0, 3.0, 4.0, and 5.0 C, respectively. Even at a high current density of 5.0 C, MNPG PP retained a high capacity of 802 mAh g^{-1}, outperforming MG PP (471 mAh g^{-1}), G PP (144 mAh g^{-1}), and PP (137 mAh g^{-1}). After the high-rate test, the cell with MNPG PP also exhibited excellent reversibility, recovering to a discharge capacity of 998.0 mAh g^{-1} upon returning to 0.1 C. These results highlight the outstanding rate capability and reversibility of the MNPG PP, which are attributed to its hierarchical structure comprising redox-mediating Mo_2C nanoparticles embedded in a heteroatom-doped amorphous carbon matrix, not serving as a high-capacity active material, but as an

efficient redox mediator (Figure S17, Supporting Information). The improved performance is further supported by enhanced LiPS conversion kinetics and Li-ion diffusion, which will be discussed in detail in the following sections.

In order to investigate the electrochemical behavior of lithium–sulfur batteries during charging and discharging, cyclic voltammetry (CV) was performed at a scan rate of 0.1 mV s^{-1} (Figure 4f). The cathodic 1st peak observed at 2.32 V is assigned to the reduction of S_8 into soluble high-order LiPS. The cathodic 2nd peak at 2.01 V corresponds to the subsequent reduction of these polysulfides into insoluble lower-order species such as Li_2S_2 and Li_2S. The anodic peak at 2.31 V represents the oxidation of Li_2S back into LiPS intermediates and eventually to S_8. The MNPG PP exhibited higher current density and a lower polarization between redox peaks compared to the other separators, indicating improved redox kinetics and efficient sulfur utilization.

To quantitatively evaluate the redox kinetics of polysulfide conversion, Tafel plots were analyzed based on the cathodic second peak (Figure 4g) and anodic peak (Figure 4h). For the cathodic second peak, the rate-determining step of LSB, the Tafel slopes of MNPG PP, MG PP, G PP, and PP were measured to be 32.9, 104.4, 123.5, and 159.7 mV dec^{-1}, respectively. The MNPG PP exhibited the lowest Tafel slope, indicating an accelerated reduction of LiPS into Li_2S. This lower value reflects a decreased kinetic barrier for the nucleation and growth of Li_2S, suggesting that the MNPG PP facilitates a more rapid LiPS conversion during discharge. The improved kinetics can be attributed to the presence of Mo_2C nanoparticles, which function as a redox mediator that promotes electron transfer and accelerates the liquid-to-solid conversion of LiPS at the MNPG PP. In the anodic region, the corresponding Tafel slopes were 65.2, 66.9, 72.9, and 78.3 mV dec^{-1} for MNPG PP, MG PP, G PP, and PP. Similarly, MNPG PP showed the lowest value, implying more efficient oxidation of Li_2S into soluble polysulfide species. The lowest Tafel slope reflects the ability of the MNPG PP to facilitate Li_2S oxidation through efficient charge transfer and regeneration of LiPS.

Figure 4i shows the cycle performance of LSBs at 0.2 C over 200 cycles. The cell with MNPG PP exhibited an initial discharge capacity of 1145.4 mAh g^{-1} and maintained 928.4 mAh g^{-1} after 200 cycles, indicating a low-capacity fading rate of 0.095% per cycle and capacity retention of 81.1%. In contrast, the cell with the PP exhibited an initial discharge capacity of 880.3 mAh g^{-1} and maintained 644.5 mAh g^{-1} after 200 cycles, corresponding to a high-capacity fading rate of 0.134% per cycle and a capacity retention of 73.2%. This enhanced cycle performance can be attributed to the synergistic effect of the heteroatom doped carbon layer and embedded Mo_2C comprising MNPG PP, which effectively suppresses degradation of redox mediators that can mitigate the LiPS shuttl. In this work, the LSBs with the MNPG PP separator achieved superior capacity and rate capability to the previously reported Mo-based modified separators, delivering a long-term cyclability (Table S3, Supporting Information).

CV measurements at varying scan rates were conducted to analyze the redox kinetics and Li-ion transport behavior of sulfur species.[38] Contour plots of CV curves measured at scan rates ranging from 0.1 to 0.5 mV s^{-1} are shown in **Figure 5**a,b for LSBs with MNPG PP and PP separators, respectively. From the contour plots, two distinct cathodic peaks and one anodic peak are observed, corresponding to the characteristic stepwise redox conversion of sulfur species. Compared to PP, the MNPG PP exhibits a sharper current response and narrower peak distribution, particularly in the low-voltage cathodic region associated with the liquid-to-solid conversion ($Li_2S_n \rightarrow Li_2S$). In addition, the redox peak positions in the MNPG PP exhibit smaller shifts with increasing scan rate, indicating reduced polarization and improved Li-ion diffusion. These features confirm that the MNPG PP enables more efficient charge transport and accelerates the electrochemical conversion of polysulfides.

To evaluate the effect of the functional separator on the electrochemical kinetics of polysulfide redox reactions, peak currents (I_p) were analyzed using the Randles–Sevcik equation as follows:

$$I_p = 2.69 \times 10^5 \times n^{1.5} \times A \times D_{Li}^{0.5} \times C_{Li} \times v^{0.5} \quad (2)$$

where I_p is the peak current, n is the electron transfer number, A is the electrode area, D_{Li} is the Li-ion diffusion coefficient, C_{Li} is the Li-ion concentration of the electrolyte, and $v^{0.5}$ is the square root of the scan rate (Figure 5a,b, and Figure S18, Supporting Information). The slope values corresponding to each redox step during discharge and charge were calculated from the linear plots of I_p versus $v^{0.5}$, as shown in Figure 5c–e. In the cathodic 1st peak, the slope of MNPG PP (0.206) was higher than those of MG PP (0.160), G PP (0.138), and PP (0.090), indicating faster Li-ion transport during the initial liquid-phase redox reaction. In the cathodic second peak, associated with the solid-phase formation of Li_2S from intermediate polysulfides, MNPG PP again exhibited the slope (0.373) compared to MG PP (0.154), G PP (0.164), and PP (0.117), confirming enhanced Li-ion diffusion during Li_2S precipitation. A similar trend was observed in the anodic step, where MNPG PP showed the highest slope value (0.428) relative to MG PP (0.279), G PP (0.331), and PP (0.252), reflecting more efficient Li_2S oxidation and reversibility during the charge process. The Mo_2C nanoparticles embedded function as redox mediators to promote rapid polysulfide conversion, while the heteroatom doped amorphous carbon matrix offers high electronic conductivity and interconnected ion diffusion pathways. This synergistic architecture effectively accelerates charge transfer and supports fast and reversible redox reactions during discharge and charge.

In addition, the Li-ion diffusion behavior was examined using the galvanostatic intermittent titration technique (GITT) analysis, as shown in Figure 5f. Each galvanostatic charge/discharge pulse was applied for 10 min, followed by a relaxation time to reach thermodynamic equilibrium (Figure S19, Supporting Information).[39] The cell with MNPG PP consistently maintained higher Li-ion diffusion coefficients (D_{Li}^+) values compared to that of the cell with PP during both discharge and charge processes. The improved D_{Li}^+ values are attributed to the enhanced electrolyte wettability and abundant ionic pathways provided by the Mo_2C redox mediators and the polar carbon matrix with heteroatom-doped surface of MNPG. This indicates that Li-ion transport is more efficient in the presence of the MNPG PP interlayer, which is beneficial for improving reaction kinetics and overall electrochemical performance. Such facilitated ion transport is expected to suppress concentration polarization and stabilize the electrode/electrolyte interface during prolonged cycling.

To investigate the impact of MNPG on LiPS conversion kinetics, in situ electrochemical impedance spectroscopy (EIS) was conducted at various depths of discharge (DOD). To approximate the thermodynamic equilibrium state of the LSBs, each discharge step was followed by a relaxation step (Figure 5g,h). The final voltage of each rest step represents the thermodynamic equilibrium potential, whereas that of

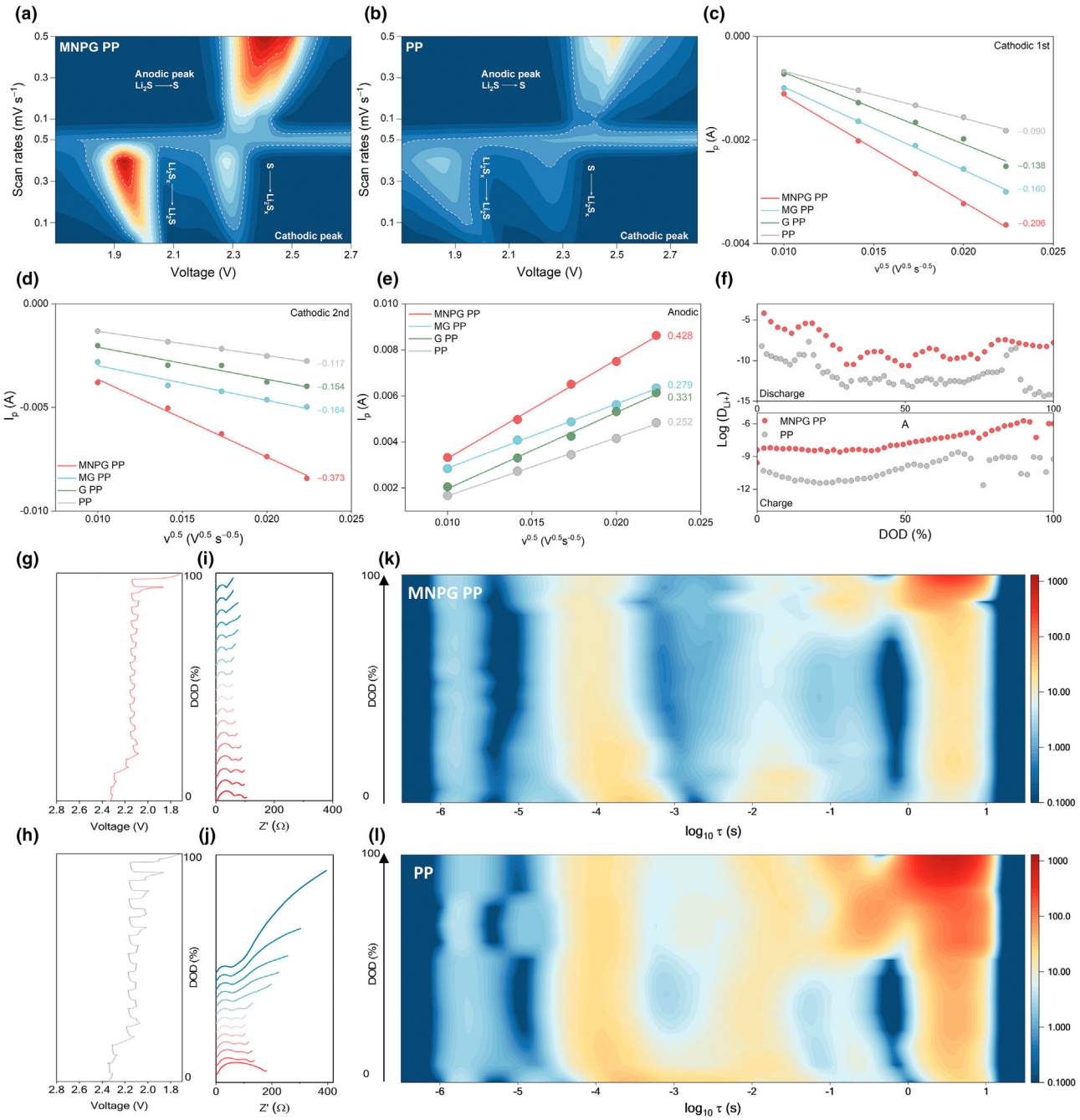

Figure 5. Contour plots of CV patterns for a) MNPG PP and b) PP under different scan rates. Peak current versus square root of scan rates of MNPG PP, MG PP, G PP, and PP at c) cathodic first, d) cathodic second, and e) anodic. f) Li-ion diffusion coefficient (D_{Li+}) of the MNPG PP and PP estimated from the galvanostatic intermittent titration technique during discharge/charge. Galvanostatic charge/discharge (GCD) profiles corresponding to in situ EIS and in situ DRT of g) MNPG PP and h) PP. i) In situ EIS plots of MNPG PP and j) PP. 2D contour plots of in situ DRT for k) MNPG PP and l) PP.

each discharge step corresponds to the kinetic potential. In the region where the liquid–solid phase transition occurs, the cell with MNPG PP exhibits a notably lower kinetic polarization compared to the pristine PP, indicating enhanced conversion kinetics. EIS was conducted at various depths of discharge, as shown in Figure 5i,j. The cell with MNPG PP exhibited consistently lower impedance across the entire discharge range, indicating improved charge transfer and ion transport behavior. Although EIS provides valuable insights into the electrochemical response during cycling, it remains limited in resolving the underlying kinetic mechanisms due to the overlapping of semicircles caused by similar time constants (τ) associated with concurrent processes. The distribution of relaxation time (DRT) spectra was further analyzed to show the kinetic contributions of individual processes across different time constant (τ) domains (Figure 5k,l and Figure S20, Supporting

Information).[40] The region corresponding to $10^{-5} < \tau < 10^{-3}$ is attributed to the solid–electrolyte interfaces at both the cathode and anode.[41] This domain is strongly influenced by the formation of an insulating Li_2S layer, which accumulates as the liquid-to-solid phase transition proceeds. Notably, the cell with MNPG PP exhibited a weaker DRT intensity in this region compared to the cell with PP, suggesting a reduced interfacial resistance. Additionally, the $10^{-3} < \tau < 10^{-1}$ range reflects the charge-transfer processes at the cathode associated with multielectron redox reactions. After the Li_2S nucleation point, the cell with MNPG PP displayed a lower charge-transfer resistance, indicating improved kinetics in the rate-determining step of the discharge process. Finally, in the region of $10^{-1} < \tau < 10^{1}$, diffusion-related processes dominate. As the discharge progresses, the amount of soluble Li_2S_6 decreases while insulating Li_2S continues to precipitate, leading to increased resistance from both Li_2S_6 and Li-ion diffusion. However, the cell with MNPG PP consistently showed lower resistance in this region as well, indicating enhanced ionic and molecular transport within the electrode.

To better explain the phase-transition-induced changes in the cell state, DRT spectra were analyzed at specific points along the discharge profile (Figure S21a, Supporting Information). The DRT peaks at various τ values are indicative of distinct polarization processes: P1 (inter-particle resistance), P2-P3 (solid-electrolyte interfacial resistance), P4-P5 (multielectron charge-transfer resistance), and P6-P7 (LiPS and bulk Li-ion diffusion). During the solid-to-liquid transition at Point A (Figure S21b, Supporting Information), the observation of P4 and P5 indicates multielectron reduction of sulfur into soluble LiPS. The appearance of P6 reflects the initiation of LiPS diffusion into the electrolyte. When the liquid-to-solid phase transition begins at Point B (Figure S21c, Supporting Information), the intensity of P4 and P5 decreases, indicating the reduced charge-transfer contribution during the conversion of soluble LiPS into insoluble species. Meanwhile, the intensity of P2 increases, which implies the nucleation of Li_2S_2/Li_2S at the cathode interface. At the end of the liquid-to-solid transition at Point C (Figure S21d, Supporting Information), P2 is significantly intensified due to extensive Li_2S accumulation. Furthermore, the intensities of P6 and P7 increased, which indicates diffusion limitations of both LiPS and Li-ion. This comprehensive DRT analysis highlights the redox-mediating functionality of MNPG and provides mechanistic insights into the evolution of LiPS conversion reactions.

3. Conclusion

In this study, we designed a multifunctional separator interlayer (MNPG PP) comprising Mo_2C nanoparticles confined within a nitrogen- and phosphorus-doped amorphous carbon matrix supported on reduced graphene oxide. The hierarchical structure was synthesized via electrostatic self-assembly and thermal transformation, enabling the formation of redox-mediating Mo_2C domains embedded within an interactive carbon shell. This architecture promotes fast and uniform Li_2S nucleation, enhances Li-ion diffusion kinetics, and suppresses parasitic reactions through synergistic interactions between the redox-mediating core and the polar doped carbon framework. Comprehensive electrochemical analyses—including Li_2S precipitation studies, symmetric cell CV, DFT adsorption modeling, and in situ EIS/DRT analysis—reveal that the MNPG interlayer not only accelerates polysulfide conversion but also regulates ion and electron transport at the interface. As a result, the cell with MNPG PP delivers a high specific capacity of 1549 mAh g^{-1} at 0.1 C, retains 802 mAh g^{-1} at 5.0 C, and maintains 81.1% capacity retention after 200 cycles. This work presents a scalable and versatile interfacial design strategy that integrates redox enhancement with diffusion control, offering new insights into the rational engineering of functional layers for high-performance LSBs.

4. Experimental Section

Synthesis of MNPG PP, MG PP, and G PP: To synthesize MNPG, 0.75 mmol of phosphomolybdic acid ($H_3PMo_{12}O_{40}$) was dissolved in 100 mL of deionized (DI) water and stirred for 5 min. Then, 40 mL of a 0.5 wt% graphene oxide (GO) solution was added and stirred for 30 min (Solution A). Separately, 1200 µL of pyrrole was dispersed in 25 mL of ethanol and sonicated for 30 min (Solution B). While maintaining vigorous stirring of Solution A, Solution B was added dropwise, followed by continuous stirring for 5 h. The resulting black solution was transferred into a Teflon-lined autoclave and subjected to hydrothermal treatment at 180 °C for 12 h. After natural cooling to room temperature, the product was washed with ethanol and DI water until a neutral pH was achieved via centrifugation. The washed sample was then freeze-dried for 72 h. The obtained powder was heat-treated at 900 °C for 2 h under an argon atmosphere to yield the final MNPG product. The MG composite was synthesized following the same procedure as MNPG, using ammonium heptamolybdate ($(NH_4)_6Mo_7O_{24}$) as the molybdenum precursor instead of phosphomolybdic acid, and glucose as the carbon source in place of pyrrole. For the preparation of reduced graphene oxide (G), 5 g of GO dispersion (2 wt%) was mixed with 5 g of hypophosphorus acid (H_3PO_2, 50 wt% aqueous solution) and 5 g of iodine (I_2) in 150 mL of DI water, as followed by stirring for 30 min. The mixture was then kept at 80 °C for 24 h. The resulting product was thoroughly washed with DI water until the filtrate reached a neutral pH, yielding the final G after freeze-drying for 72 hours.

To fabricate MNPG-PP, MNPG and PVDF were mixed at a weight ratio of 1:9 and dispersed in N-methyl-2-pyrrolidone (NMP). The resulting solution was vacuum-filtered onto a polypropylene (PP) separator to achieve a coating mass loading of 0.5 mg cm^{-2}. The sample was then dried overnight in an oven to obtain MNPG-coated PP (MNPG-PP). Similarly, MG PP and G PP were prepared using the same coating procedure.

Materials characterization: The high-resolution scanning electron microscopy (HR SEM, MERLIN) and transmission electron microscopy (TEM, Libra 200 HT Mc Cs, 200 kV) images were collected to determine the microstructure. The X-ray diffraction (XRD, D8, Bruker) was analyzed in a 2θ range of from 5° to 85° to obtain inherent peaks. Raman spectroscopy (SENTERRA Raman) was used with a 532 nm laser to confirm structural properties. Thermogravimetric analysis (TGA, SDT Q600) was measured at a heating rate of 10 °C min^{-1} in N_2 gas.

Electrode preparation and electrochemical measurements: The sulfur active material was prepared by mixing carbon nanotubes (CNTs) with sulfur at a weight ratio of 1:3, followed by melt-diffusion at 155 °C for 12 h under argon to yield CNT–S. A slurry was then prepared by dispersing CNT–S (80 wt%), PVDF (10 wt%), and carbon black (10 wt%) in NMP. This slurry was cast onto aluminum foil using a doctor blade to achieve an areal loading of 2 mg cm^{-2} and dried overnight at 80 °C to fabricate CNT–S cathodes. Coin cells (CR2032 type) were assembled using lithium metal as the anode, MNPG-PP as the separator, and CNT–S as the cathode. The electrolyte consisted of 1 M LiTFSI dissolved in a 1:1 (v/v) mixture of 1,3-dioxolane and 1,2-dimethoxyethane with 2 wt% $LiNO_3$ additive. The specific capacity was calculated based on 1C = 1675 mA g^{-1}.

Li_2S nucleation test and Li_2S_6 symmetric cell test: To prepare the MNPG electrode, MNPG (80 wt%), PVDF (10 wt%), and carbon black (10 wt%) were dispersed in NMP to form a slurry. The slurry was coated onto aluminum foil using a doctor blade to a loading of 1 mg cm^{-2} and dried overnight at 80 °C. For the Li_2S nucleation test, 30 µL of 0.5 M Li_2S_8-containing electrolyte was added to the cathode side and 30 µL of Li_2S_8-free electrolyte to the anode side. The cell was first discharged galvanostatically to 2.10 V at 0.05 C, followed by potentiostatic discharge at 2.10 V to monitor Li_2S nucleation and growth. For the Li_2S_6 symmetric cell test, the same MNPG electrode was assembled into a symmetric cell configuration with 30 µL of 0.5 M Li_2S_6-containing electrolyte. The cell was tested in a voltage range of −1 to 1 V.

Computational details: Density functional theory (DFT) calculations were performed with the Vienna Ab initio Simulation Package (VASP).[42] Projector-

augmented wave pseudopotentials were used with a plane-wave basis set, as implemented in VASP.[43] Perdew–Burke–Ernzerhof's (PBE) parametrization of the generalized gradient approximation (GGA) was used.[44] A $2 \times 2 \times 1$ k-point grid was used for DFT calculations to calculate the Mo_2C surface. For more accurate calculation results for van der Waals interaction between lithium polysulfide and substrate, the DFT-D3 correction method was considered in this study.[45] A kinetic energy cutoff of as 500 eV was used in all the calculations, and the overall structure was optimized until the force in the unit cell converged to within 0.03 eV $Å^{-1}$.

In situ distribution of relaxation times analysis: Galvanostatic discharge was conducted for 10 minutes, followed by a 30-minute relaxation step. After each relaxation step, electrochemical impedance spectroscopy (EIS) was measured over a frequency range from 1×10^6 Hz to 0.01 Hz using a Bio-Logic VMP3 potentiostat/galvanostat. The DRT analysis was carried out using an open-source MATLAB code,[46] where Tikhonov regularization was applied along with a Gaussian-based discretization approach. Both real and imaginary parts of the impedance spectra were included in the fitting, while inductive components were excluded. A first-order derivative regularization was used with the regularization parameter set to 1×10^{-3}. Radial basis functions with a full width at half-maximum (FWHM) of 0.5 were employed, enabling accurate fitting of the DRT spectra.

Acknowledgments

W.I.K. and M.J.K. contributed equally to this work. This work was supported by the National Research Foundation of Korea (NRF) grant funded by the Korea government (MSIT) (no. RS-2023-00217581) and a grant (RS-2024-00470023) from the Materials and Components Technology Development (R&D) Project funded by the Ministry of Trade, Industry and Energy of the Republic of Korea.

Conflict of Interest

The authors declare no conflict of interest.

Supporting Information

Supporting Information is available from the Wiley Online Library or from the author.

Keywords

lithium sulfur batteries, molybdenum carbide, redox mediators, separator modifications

Received: July 19, 2025
Revised: August 22, 2025
Published online: August 25, 2025

[1] A. Manthiram, Y. Fu, S. H. Chung, C. Zu, Y. S. Su, *Chem. Rev.* **2014**, *114*, 11751.
[2] Z. W. Seh, Y. Sun, Q. Zhang, Y. Cui, *Chem. Soc. Rev.* **2016**, *45*, 5605.
[3] G. Zhou, H. Chen, Y. Cui, *Nat. Energy* **2022**, *7*, 312.
[4] M. Jana, R. Xu, X.-B. Cheng, J. S. Yeon, J. M. Park, J.-Q. Huang, Q. Zhang, H. S. Park, *Energy Environ. Sci.* **2020**, *13*, 1049.
[5] J. S. Yeon, S. Yun, J. M. Park, H. S. Park, *ACS Nano* **2019**, *13*, 5163.
[6] H.-Y. Park, S. H. Kim, J.-H. Yu, J. E. Kwon, J. Y. Lim, S. W. Choi, J.-S. Yu, Y. Jung, *J. Electrochem. Sci. Technol.* **2024**, *15*, 198.
[7] W. Hua, T. Shang, H. Li, Y. Sun, Y. Guo, J. Xia, C. Geng, Z. Hu, L. Peng, Z. Han, C. Zhang, W. Lv, Y. Wan, *Nat. Catal.* **2023**, *6*, 174.
[8] S. Zhou, J. Shi, S. Liu, G. Li, F. Pei, Y. Chen, J. Deng, Q. Zheng, J. Li, C. Zhao, I. Hwang, C. J. Sun, Y. Liu, Y. Deng, L. Huang, Y. Qiao, G. L. Xu, J. F. Chen, K. Amine, S. G. Sun, H. G. Liao, *Nature* **2023**, *621*, 75.
[9] Z. Shen, X. Jin, J. Tian, M. Li, Y. Yuan, S. Zhang, S. Fang, X. Fan, W. Xu, H. Lu, J. Lu, H. Zhang, *Nat. Catal.* **2022**, *5*, 555.
[10] M. J. M. Al Essa, *J. Electrochem. Sci. Technol.* **2024**, *15*(1), 1.
[11] Z. Li, I. Sami, J. Yang, J. Li, R. V. Kumar, M. Chhowalla, *Nat. Energy* **2023**, *8*, 84.
[12] Y. Lan, Y. Wang, Y. Wang, G. Lu, L. Liu, T. Tang, M. Li, Y. Cheng, J. Xiao, X. Li, *ACS Nano* **2024**, *18*, 15638.
[13] S. Kim, W. G. Lim, H. Jung, Y. C. Jeong, C. Y. Park, S. B. Yang, C. H. Lee, D. Wang, K. Sohn, J. W. Han, J. Lee, *Nat. Commun.* **2025**, *16*, 1649.
[14] L. Guan, H. Hu, L. Li, Y. Pan, Y. Zhu, Q. Li, H. Guo, K. Wang, Y. Huang, M. Zhang, Y. Yan, Z. Li, X. Teng, J. Yang, J. Xiao, Y. Zhang, X. Wang, M. Wu, *ACS Nano* **2020**, *14*, 6222.
[15] X. Zuo, M. Zhen, D. Liu, L. Fu, Y. Qiu, H. Liu, Y. Zhang, *Adv. Funct. Mater.* **2024**, *34*, 2309840.
[16] Y. Kim, W. I. Kim, H. Park, J. S. Kim, H. Cho, J. S. Yeon, J. Kim, Y. J. Kim, J. Lee, H. S. Park, *Adv. Energy Mater.* **2023**, *13*, 2204353.
[17] L. Peng, Z. Wei, C. Wan, J. Li, Z. Chen, D. Zhu, D. Baumann, H. Liu, C. S. Allen, X. Xu, A. I. Kirkland, I. Shakir, Z. Almutairi, S. Tolbert, B. Dunn, Y. Huang, P. Sautet, X. Duan, *Nat. Catal.* **2020**, *3*, 762.
[18] X. Yu, Y. Kang, H. S. Park, *Carbon* **2016**, *101*, 49.
[19] W. Xia, M. Cheng, J. Hu, Q. Liu, T. Wei, R. Wang, W. Li, B. Liu, *Carbon Lett.* **2024**, *34*, 85.
[20] J. Lei, X. X. Fan, T. Liu, P. Xu, Q. Hou, K. Li, R. M. Yuan, M. S. Zheng, Q. F. Dong, J. J. Chen, *Nat. Commun.* **2022**, *13*, 202.
[21] W. I. Kim, J. S. Yeon, H. Park, H. J. Kim, M. J. Kim, J. Kim, H. S. Park, *Compos. Part B* **2023**, *264*, 110886.
[22] J. S. Li, Y. Wang, C. H. Liu, S. L. Li, Y. G. Wang, L. Z. Dong, Z. H. Dai, Y. F. Li, Y. Q. Lan, *Nat. Commun.* **2016**, *7*, 11204.
[23] C. Wu, J. Li, *ACS Appl. Mater. Interfaces* **2017**, *9*, 41314.
[24] W. Dai, L. Lu, Y. Han, L. Wang, J. Wang, J. Hu, C. Ma, K. Zhang, T. Mei, *ACS Omega* **2019**, *4*, 4896.
[25] H. J. Peng, J. Q. Huang, M. Q. Zhao, Q. Zhang, X. B. Cheng, X. Y. Liu, W. Z. Qian, F. Wei, *Adv. Funct. Mater.* **2014**, *24*, 2772.
[26] J. Wan, J. Wu, X. Gao, T. Li, Z. Hu, H. Yu, L. Huang, *Adv. Funct. Mater.* **2017**, *27*, 1703933.
[27] L. Zhi, H. Xia, G. Feng, H. Cao, X. Xu, S. Zhang, J. Li, P. Zhang, *J. Phys. Chem. Solids* **2025**, *199*, 112560.
[28] J. Tan, X. He, F. Yin, X. Liang, B. Chen, G. Li, H. Yin, *J. Mater. Sci.* **2018**, *54*, 4589.
[29] X. Hu, M. Fan, Y. Zhu, Q. Zhu, Q. Song, Z. Dong, *Green Chem.* **2019**, *21*, 5274.
[30] X. Wang, M. Niu, C. Gao, Y. Li, T. Li, B. Ren, *Carbon Lett.* **2024**, *34*, 1385.
[31] Z. Li, Y. Zhou, Y. Wang, Y. C. Lu, *Adv. Energy Mater.* **2018**, *9*, 1802207.
[32] B. Wang, L. Wang, B. Zhang, S. Zeng, F. Tian, J. Dou, Y. Qian, L. Xu, *ACS Nano* **2022**, *16*, 4947.
[33] H. Yuan, J. Zheng, G. Lu, L. Zhang, T. Yan, J. Luo, Y. Wang, Y. Liu, T. Guo, Z. Wang, J. Nai, X. Tao, *Adv. Mater.* **2024**, *36*, e2400639.
[34] X.-B. Cheng, Q. Zhang, H.-F. Wang, G.-L. Tian, J.-Q. Huang, H.-J. Peng, M.-Q. Zhao, F. Wei, *Catal. Today* **2015**, *249*, 244.
[35] D. A. C. Eduardo Cruz-Silva, L. Gu, M. Terrones, *ACS Nano* **2008**, *2*, 441.
[36] X. Wu, N. Liu, Z. Guo, M. Wang, Y. Qiu, D. Tian, B. Guan, L. Fan, N. Zhang, *Energy Storage Mater* **2020**, *28*, 153.
[37] J. B. Lee, G. Min, W.-G. Lim, H. Kang, K. Shin, S. Yoon, J. Lee, J. Joo, *Korean J. Chem. Eng.* **2024**, *41*, 1239.
[38] R. Gao, M. Zhang, Z. Han, X. Xiao, X. Wu, Z. Piao, Z. Lao, L. Nie, S. Wang, G. Zhou, *Adv. Mater.* **2024**, *36*, e2303610.
[39] Z. X. Chen, Q. Cheng, X. Y. Li, Z. Li, Y. W. Song, F. Sun, M. Zhao, X. Q. Zhang, B. Q. Li, J. Q. Huang, *J. Am. Chem. Soc.* **2023**, *145*, 16449.

[40] Y. Lu, C.-Z. Zhao, J.-Q. Huang, Q. Zhang, *Joule* **2022**, *6*, 1172.
[41] R. Soni, J. B. Robinson, P. R. Shearing, D. J. L. Brett, A. J. E. Rettie, T. S. Miller, *Energy Storage Mater* **2022**, *51*, 97.
[42] G. Kresse, J. F. Furthmüller, *Comput. Mater. Sci.* **1996**, *6*, 15.
[43] P. E. Blochl, *Phys. Rev. B Condens. Matter* **1994**, *50*, 17953.
[44] P. John, K. B. Perdew, M. Ernzerhof, *Phys. Rev. Lett.* **1996**, *77*, 3865.
[45] S. Grimme, J. Antony, S. Ehrlich, H. Krieg, *J. Chem. Phys.* **2010**, *132*, 154104.
[46] T. H. Wan, M. Saccoccio, C. Chen, F. Ciucci, *Electrochim. Acta* **2015**, *184*, 483.